



**HAL**  
open science

# Performance of a miniature high-temperature superconducting (HTS) surface coil for in vivo microimaging of the mouse in a standard 1.5T clinical whole-body scanner

Marie Poirier-Quinot, Jean-Christophe Ginefri, Olivier Girard, Philippe Robert, Luc Darrasse

## ► To cite this version:

Marie Poirier-Quinot, Jean-Christophe Ginefri, Olivier Girard, Philippe Robert, Luc Darrasse. Performance of a miniature high-temperature superconducting (HTS) surface coil for in vivo microimaging of the mouse in a standard 1.5T clinical whole-body scanner. *Magnetic Resonance in Medicine*, 2008, 60 (4), pp.917-927. 10.1002/mrm.21605 . hal-02270035

**HAL Id: hal-02270035**

**<https://hal.science/hal-02270035>**

Submitted on 28 Oct 2021

**HAL** is a multi-disciplinary open access archive for the deposit and dissemination of scientific research documents, whether they are published or not. The documents may come from teaching and research institutions in France or abroad, or from public or private research centers.

L'archive ouverte pluridisciplinaire **HAL**, est destinée au dépôt et à la diffusion de documents scientifiques de niveau recherche, publiés ou non, émanant des établissements d'enseignement et de recherche français ou étrangers, des laboratoires publics ou privés.

# Performance of a Miniature High-Temperature Superconducting (HTS) Surface Coil for In Vivo Microimaging of the Mouse in a Standard 1.5T Clinical Whole-Body Scanner

Marie Poirier-Quinot,<sup>1\*</sup> Jean-Christophe Ginefri,<sup>1</sup> Olivier Girard,<sup>1</sup> Philippe Robert,<sup>2</sup> and Luc Darrasse<sup>1</sup>

**The performance of a 12-mm high-temperature superconducting (HTS) surface coil for in vivo microimaging of mice in a standard 1.5T clinical whole-body scanner was investigated. Systematic evaluation of MR image quality was conducted on saline phantoms with various conductivities to derive the sensitivity improvement brought by the HTS coil compared with a similar room-temperature copper coil. The observed signal-to-noise ratio (SNR) was correlated to the loaded quality factor of the radio frequency (RF) coils and is theoretically validated with respect to the noise contribution of the MR acquisition channel. The expected in vivo SNR gain was then extrapolated for different anatomical sites by monitoring the quality factor in situ during animal imaging experiments. Typical SNR gains of 9.8, 9.8, 5.4, and 11.6 were found for brain, knee, back, and subcutaneous implanted tumors, respectively, over a series of mice. Excellent in vivo image quality was demonstrated in 16 min with native voxels down to (59  $\mu\text{m}$ )<sup>3</sup> with an SNR of 20. The HTS coil technology opens the way, for the first time at the current field strength of clinical MR scanners, to spatial resolutions below 10<sup>-3</sup> mm<sup>3</sup> in living mice, which until now were only accessible to specialized high-field MR microscopes. Magn Reson Med 60: 917–927, 2008. © 2008 Wiley-Liss, Inc.**

**Key words:** MR microscopy; high-temperature superconductor (HTS); miniature radiofrequency (RF) coil; clinical whole-body scanner; small animal, mouse

In the context of the growing interest for physiological and pathological models with small rodents such as mice and rats, an emerging trend to perform high-resolution imaging has been to involve standard clinical whole-body MR scanners (e.g., 1–13) as an alternative to currently used more specialized high-field systems (14). An argument for this approach is the widespread implementation of clinical MR facilities already equipped with standardized protocols. Thus, the transfer between animal and clinical imaging protocols is easy, and the need for additional investments is limited. In addition, there is a fundamental motivation to investigate animal models using the common magnetic field of most clinical scanners since the MR

contrast characteristics significantly depend on the field strength. Finally, the wide-bore magnet offers the advantage of simultaneously imaging multiple animals within the same MRI unit (15,16).

Intrinsically, specialized high-field MRI systems are well suited for high-resolution studies on small animals because they are equipped with small-bore gradient systems able to reach large amplitudes, which readily give fast access to high spatial frequency information. Alternatively, the accessible spatial resolution with a whole-body clinical scanner is inherently low unless either a longer observation time window (1) or an enhanced gradient insert (7,11) are implemented. However, the built-in whole-body gradient systems of new generation scanners can now deliver 50 mT/m amplitudes at switching speeds of a few 100  $\mu\text{s}$ , which potentially allow decreasing the voxel size down to less than 100  $\mu\text{m}$  isotropic within an encoding time of 5 ms. Thus, the spatial encoding effectiveness of clinical whole-body scanners tends to no longer be a strong limitation for microimaging investigations in small animals.

The actual issue in achieving spatial resolutions approaching 10<sup>-3</sup> mm<sup>3</sup> with clinical scanners today is the low signal-to-noise ratio (SNR) available at the typical field strength of 1.5T. The use of a specially designed radio frequency (RF) coil that fits the animal is then required to compensate for the SNR loss resulting from the small voxel size. Still, scan times of several dozen minutes may be required to get an acceptable SNR. This makes in vivo animal handling difficult and is incompatible with dynamic studies.

The purpose of the present work was to address the improvement brought by new superconducting RF coil technology (17) in the situation of a miniature surface coil suited for regional microimaging of mice in a 1.5T scanner. Reducing the sensitive volume of the RF coil is a way to increase the MR signal due to stronger magnetic coupling between the coil windings and the observed protons. Additionally, it filters out the RF noise from the rest of the body, resulting in a very efficient method to locally increase the SNR. However, at 64 MHz, the noise arising from the RF coil itself clearly dominates the sample noise in the case of conventional room-temperature copper coils of typical diameters smaller than 2 to 3 cm. Therefore, designing the coil with high-temperature superconducting (HTS) material that features extremely low intrinsic noise can hold promise to dramatically improve the SNR. Small-animal investigations with either cooled-copper or HTS

<sup>1</sup>U2R2M (UMR8081), University of Paris-Sud, Centre National de la Recherche Scientifique (CNRS), Orsay, France.

<sup>2</sup>Guerbet Research, Aulnay-Sous-Bois, France.

Grant sponsors: French Ministry of Research, RNTS Program; IPA Joint Program, Centre National de la Recherche Scientifique (CNRS)–Commissariat à l'Énergie Atomique (CEA).

\*Correspondence to: Marie Poirier-Quinot, U2R2M, Bat 220, Univ Paris-Sud, Orsay F 91405, France. E-mail: marie.poirier-quinot@u-psud.fr

Received 7 March 2007; revised 12 January 2008; accepted 1 February 2008.

DOI 10.1002/mrm.21605

Published online in Wiley InterScience (www.interscience.wiley.com).

coils have already been reported, either in MR microscopes (18–22) or in standard clinical scanners at moderate spatial resolution (23–25). Comparisons with room-temperature copper coils have demonstrated SNR gains ranging from two to four times in vivo (21–25) and up to 10 times on very small anatomical pieces (18,19). Here, an even smaller HTS surface coil with a diameter of about 1 cm is considered in view of the mouse imaging application on a commercially available 1.5T whole-body MR scanner. Particular attention is focused on the design of electrical matching between the RF coil and the receiver input of the scanner, which is crucial for the actual performance of the HTS coil due to the loaded quality factors of several thousands observed with the mouse. The probe head is adapted from a previous design dedicated to local microimaging of human skin (26). Preliminary investigations on intact excised organs (27) and in a mouse (28–30) have been partially reported.

As stressed in a review article (17), evaluations of the SNR gain brought by an HTS coil are generally quite unfair, mainly because of the arbitrary choice both of the geometry of the reference copper coil and of its position relative to the sample. Moreover, sufficient experimental data are most often lacking to unambiguously assess the comparison. Strong emphasis has therefore been put here on the method used to compare HTS and copper coils. Almost identical geometries have been chosen in order to achieve the same spatial sensitivity distribution in both cases. The method accounts for potential biases, i.e., flip angle misadjustment and slice profile distortion, that arise from the nonlinear behavior of HTS coils (18). In addition, direct comparison of SNR measurements on in vivo MR images was found to be insufficiently reliable due to the inaccuracy of animal repositioning, the instability of physiological conditions, and the presence of motion artifacts. Therefore, systematic comparison of MR images has been conducted with saline phantoms of variable conductivity, and the observed SNR has been correlated with the corresponding electrical quality factor of the RF coil. Extrapolation of the expected SNR gain in vivo is then possible by monitoring the quality factor in situ during any animal imaging experiment and by including the noise contribution of the preamplifier and coupling device. The SNR gain has been evaluated for different anatomical sites (brain, knee, back, and subcutaneous implanted tumors) over a series of mice. The Results section also displays MR views of the different sites, which are representative of the image quality achievable with the HTS coil.

## THEORY

The SNR of an MR image can be expressed for a given RF coil geometry as a function of  $Q_l$ ,  $Q_u$ , the loaded and unloaded quality factors of the RF coil, respectively, and  $T_c$ ,  $T_s$ , the RF coil and sample temperatures, respectively:

$$SNR_{\infty} \propto \sqrt{\frac{Q_l}{T_s \left(1 - \frac{Q_l}{Q_u}\right) + T_c \frac{Q_l}{Q_u}}}. \quad [1]$$

The noise contribution from a conventional 50- $\Omega$  preamplifier can be evaluated by comparing pure noise im-

ages acquired with a 50- $\Omega$  load connected to the preamplifier input at two different temperatures  $T_a$  and  $T_b$  (31). From the corresponding standard noise deviations  $\sigma_a$  and  $\sigma_b$ , the standard preamplifier noise temperature  $T_N$  is given by:

$$T_N = \frac{T_a - \left(\frac{\sigma_a}{\sigma_b}\right)^2 T_b}{\left(\frac{\sigma_a}{\sigma_b}\right)^2 - 1} \quad [2]$$

When the RF coil is perfectly matched to the preamplifier input, the SNR degradation is simply accounted for by adding the term  $T_N$  in the denominator of Eq. [1] (32). However, matching the resonant RF coil to the preamplifier input cannot be perfectly achieved at any frequency offset due to the frequency-dependent reactance. Since HTS coils exhibit very high quality factors, the mismatch is particularly critical and may result in visible image SNR degradation with position dependence along the frequency-encoded (readout) direction.

In practice, inductive coupling techniques based on a tuned secondary coil, such as described in Fig. 1, provide an easy way to wirelessly match the RF coil to the preamplifier. Such an approach avoids introducing a thermal sink into the cryostat. However, the thermal noise from the coupling coil increases the total receiver noise power by a factor  $F_{cc}$  (33). An approximate expression of  $F_{cc}$  can be given as a function of the MR signal frequency  $\omega$ :

$$F_{cc} = 1 + \frac{T_{cc}}{T_{eff} k^2 Q_{cc} Q_l} \left[ 1 + Q_l^2 \left( 1 - \frac{\omega_0^2}{\omega^2} \right)^2 \right] \\ \text{with } T_{eff} = T_s \left( 1 - \frac{Q_l}{Q_u} \right) + T_c \frac{Q_l}{Q_u}, \quad [3]$$

where  $k$  is the magnetic coupling coefficient between RF and coupling coils,  $Q_{cc}$ ,  $r_{cc}$ , and  $T_{cc}$  are the quality factor, equivalent series resistance, and temperature of the coupling coil, respectively, and  $T_{eff}$  is the effective temperature of the HTS coil.

The noise contribution from the preamplifier is minimized when the output impedance,  $Z_{out}$ , is equal to the optimal source impedance,  $Z_0$ , of the preamplifier (usually

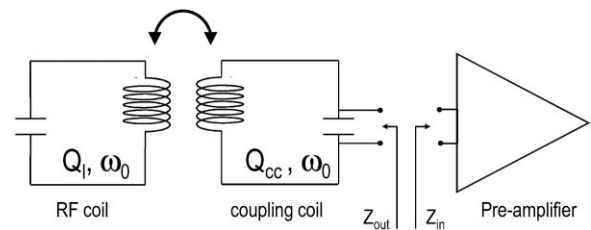


FIG. 1. Basic scheme of the inductively coupled double-resonant reception.  $Q_l$  and  $Q_{cc}$  are the quality factors of the RF coil and the coupling coil, respectively. The two coupled circuits are independently tuned to the Larmor frequency  $\omega_0$ .  $Z_{out}$  is the impedance of the RF coil viewed from the output of the matching circuit and set by adjusting the coupling coefficient.  $Z_{in}$  is the input impedance of the preamplifier.

50  $\Omega$ ). Using the virtual reflection coefficient  $\rho$  to describe the impedance mismatch between  $Z_{out}$  and  $Z_0$  at offset frequencies ( $\omega \neq \omega_0$ ), the noise from the preamplifier contributes to the output noise power by the factor  $F_p$  (17,34):

$$F_p = 1 + \frac{T_N 1 + |\rho|^2}{T_{eq} 1 - |\rho|^2} \quad [4]$$

with

$$\rho = \frac{Z_0 - Z_{out}}{Z_0 + Z_{out}} \text{ and } T_{eq} = \frac{F_{cc} T_{eff}}{1 + (F_{cc} - 1) \frac{T_{eff}}{T_{cc}}}$$

where  $T_{eq}$  is the effective temperature of the matched HTS coil circuit including the coupling coil. The impedance  $Z_{out}$  achieved with the second-order coupling circuit of Fig. 1 is given by:

$$Z_{out} = \frac{bc r_{cc}}{\left(-c + a \frac{\omega^2}{\omega_0^2}\right)^2 + \frac{b^2 \omega^4}{Q_{cc}^2 \omega_0^4}} + j \frac{Q_{cc} r_{cc} \left(ac - \left(a^2 + \frac{b^2}{Q_{cc}^2}\right) \frac{\omega^2}{\omega_0^2}\right)}{\left(-c + a \frac{\omega^2}{\omega_0^2}\right)^2 + \frac{b^2 \omega^4}{Q_{cc}^2 \omega_0^4}} \quad [5]$$

with

$$a = 1 + Q_l^2 \left(1 - \frac{\omega_0^2}{\omega^2}\right)^2 - k^2 Q_l^2 \left(1 - \frac{\omega_0^2}{\omega^2}\right)$$

$$b = 1 + Q_l^2 \left(1 - \frac{\omega_0^2}{\omega^2}\right)^2 + k^2 Q_l Q_{cc}$$

$$c = 1 + Q_l^2 \left(1 - \frac{\omega_0^2}{\omega^2}\right)^2,$$

Assuming  $r_{cc} \ll Z_0 \ll Q_{cc}^2 r_{cc}$ , the matching condition  $Z_{out} = Z_0$  can be reached at a frequency close to  $\omega_0$  by setting  $k^2 \approx Q_{cc} r_{cc} / Q_l Z_0$ . The SNR initially given by the RF coil (Eq. [1]) is degraded at the receiver output by a factor  $F_{tot}^{1/2}$ , where  $F_{tot}$  is the product of the contributions  $F_{cc}$  from the coupling coil and  $F_p$  from the preamplifier.

Finally, the circuit of Fig. 1 also transforms the MR signal induced in the RF coil (33), acting as a filter on both the signal and noise with a frequency response  $G$  approximated by:

$$G \approx \frac{Z_{in}}{Z_{in} + Z_{out}} \frac{k^2 Q_{cc} Q_l}{k^2 Q_{cc} Q_l - Q_l Q_{cc} \left(1 - \frac{\omega_0^2}{\omega^2}\right)^2 + j(Q_l + Q_{cc}) \left(1 - \frac{\omega_0^2}{\omega^2}\right)}. \quad [6]$$

Due to the frequency dependence of  $Z_{out}$ , the response  $G$  may be strongly affected depending on the load impedance  $Z_{in}$  at the coupling coil output. For coil array decoupling

purposes (35), most recent MRI systems are equipped with dedicated preamplifiers featuring an input impedance an order of magnitude larger or smaller than their optimal source impedance  $Z_0$ . Since the input impedance differs from  $Z_0$ , inserting a transmission cable between the preamplifier input and the coupling-coil output may introduce an additional impedance transformation, which must be considered for practical implementation. Noticeably, the present SNR model (Eqs. [3]–[5]) remains valid assuming a lossless transmission line of characteristic impedance equal to  $Z_0$ .

## MATERIALS AND METHODS

### MRI System and RF Monitoring Hardware

The experimental work was performed on a standard clinical whole-body 1.5T MR scanner (Signa; GE Medical Systems, Milwaukee, WI, USA). The scanner can deliver a maximum gradient intensity of 22 mT/m with a rise time of 288  $\mu$ s. Both HTS and copper coils were used in transmit/receive mode. Electrical connection to the MR scanner was implemented by plugging a 50- $\Omega$  coaxial cable, with a length equal to a quarter-wavelength ( $\lambda/4$ ), into the standard bayonet nut coupling (BNC) input of the manufacturer's "Extremity Coil" fast connection box. A load impedance,  $Z_{in}$ , of 450  $\Omega$  was measured with an impedance probe (HP 41941-61001; Hewlett-Packard) at the  $\lambda/4$ -cable end, corresponding to about 5.5  $\Omega$  at the fast connection box input. For each operating condition, impedance matching at the RF coil output was monitored inside the magnet bore before connection using an additional coaxial cable and an impedance analyzer (HP4194A; Hewlett-Packard) placed 5 m away from the magnet. Matching was adjusted to 50  $\Omega$  at an RF source level of  $-30$  dBm, which was low enough to observe a linear response with the HTS coil. The quality factors  $Q_u$  and  $Q_l$  were extracted during this step using swept-frequency analysis of the RF coil impedance.

The equivalent noise temperature of the receiver input available within the fast connection box was evaluated by the dual-temperature method, Eq. [2], at 293 K (room temperature) and 77 K (liquid nitrogen temperature). Standard deviations  $\sigma_a$  and  $\sigma_b$  of  $6.27 \pm 0.06$  and  $3.85 \pm 0.1$  (mean  $\pm$  standard deviation) were extracted from a series of six pure noise images, acquired using a 2D spin-echo sequence with repetition time (TR) = 300 ms, echo time (TE) = 9 ms, field of view (FOV) =  $8 \times 8$  cm<sup>2</sup>, matrix size =  $256 \times 128$ , acquisition bandwidth (BW) = 30.5 Hz/pixel, and acquisition time ( $t_{acq}$ ) = 44 s. An equivalent noise temperature  $T_N$  of  $57 \pm 15$  K was found, which corresponds to a noise figure of 0.78 dB.

### RF Coils

The HTS and copper surface coils were identical except for different conducting/superconducting layers and different operating temperatures. The design was a five-turn transmission line resonator (36) with inner and outer radii of 4.5 mm and 7.3 mm, respectively. Geometric parameters that set the resonance frequency within a few percent have been detailed previously (26).

The windings of the HTS coil are made of a 400-nm-thick YBaCuO film deposited and etched on a LaAlO<sub>3</sub>

substrate by Thomson-L.C.R. (Corbeville, France) (37). The HTS coil was operated at about 80 K, using a nonmagnetic liquid-nitrogen cryostat (Desert Cryogenics, LLC, Tucson, AZ, USA) specially designed with a sapphire cold finger to allow lateral access to large samples (27). The cryostat, a tubular cylinder with a diameter of 50 mm and length of 300 mm, was attached to the patient bed by an adjustable plastic support. It was maintained at a 45° oblique orientation in the vertical plane parallel to the static magnetic field to provide stable MRI operation with autonomous cooling for up to 5 h. The HTS coil was mounted in the secondary-vacuum chamber of the cryostat onto a sapphire plate with a thickness of 500  $\mu\text{m}$ , which was connected at right angle to a  $10 \times 10 \text{ mm}^2$  sapphire rod plugged into the cold nitrogen reservoir. Separation from the room-temperature outside surface was insured by a 500- $\mu\text{m}$ -thick sapphire window and a 500- $\mu\text{m}$  minimum insulation gap in the secondary vacuum. The overall distance between the HTS coil plane and the sample surface was about 2 mm, including the additional spacing needed for the tuning and matching setup described below. The unloaded quality factor  $Q_u$  was greater than 62,000 in the Earth's magnetic field, and decreased to 13,700 when the HTS coil was placed at the center of the 1.5T magnet. This lower value was not due to the coupling of the RF coil to outer structures but rather due to the direct modification of the RF resistivity of the HTS material by the strong static magnetic field. Influence of the static field was tested on measurements done after a quench of the MRI magnet, for which the same high value of  $Q_u$  was found both outside and inside the bore of the off magnet.

The copper coil was made of 15- $\mu\text{m}$  thick copper electrodeposited on  $\text{LaAlO}_3$  by an ultraviolet micromolding process (38). The copper coil had a  $Q_u = 110$  at room temperature. The overall gap between the copper coil

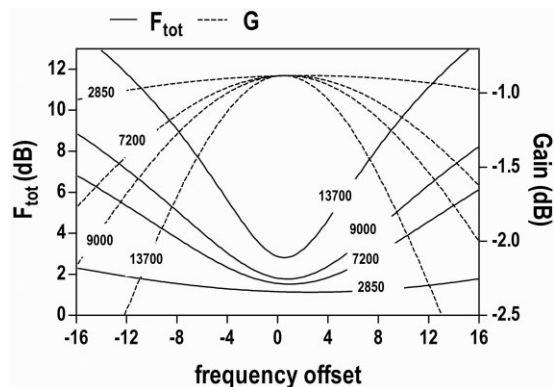


FIG. 2. Expected gain flatness ( $G$ ) and SNR degradation ( $F_{tot}$ ) with the coupling network of Fig. 1 for the unloaded HTS coil ( $Q_u = 13,700$ ) and for different loaded- $Q$  values (9000, 7200, 2850). Both receiver gain and SNR are affected by the frequency-dependent impedance mismatch at the preamplifier input. The SNR degradation accounts for noise contributions from both the preamplifier and coupling devices compared to the noise source from the HTS coil. The SNR-degradation profiles appear generally sharper than the gain flatness, resulting in a background-noise profile with a minimum close to the zero frequency offset. For the copper coil (not shown), the SNR degradation stays almost constant at about 0.96 dB.

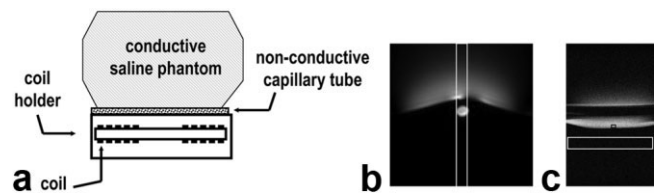


FIG. 3. a: SNR calibration phantoms. Phantoms were made of a catheter filled with distilled water and a 500-ml saline perfusion bag. NaCl concentration in the perfusion bag was varied to produce a set of different RF coil loading conditions. Coronal slice (b) and axial slice (c) performed with the HTS coil for the phantom at  $[\text{NaCl}] = 154 \text{ mM}$ . The SNR was measured on the axial slice with voxels of  $39 \times 39 \times 900 \mu\text{m}^3$ . The target ROI (black) encompassed  $10 \times 10$  pixels and the background ROI (white),  $40 \times 200$  pixels.

plane and the sample surface was about 1 mm using the same tuning and matching setup as for the HTS coil.

Both coils were initially designed to resonate slightly above (typically 3%), and then retuned to within 20 kHz below the Larmor frequency. Retuning was achieved by partially overlapping the windings on one side of the coil with a thin dielectric pad (polytetrafluoroethylene [PTFE] and sapphire for the HTS and copper coils, respectively). This step had no relevant effect on the quality factor. Fine tuning was finally achieved by positioning a closed-circuit copper loop with a diameter of 12 mm. Upward frequency shifts up to 20 kHz could be induced without significantly affecting the coil quality factor.

Matching the source impedance,  $Z_0$ , of 50  $\Omega$  was achieved by another 12-mm diameter copper loop (Fig. 1), with  $Q_{cc}$  around 75 at room temperature, tuned at the Larmor frequency with a 150-pF capacitor. Figure 2 displays the receiver gain flatness  $G$  resulting from the frequency response of the matching network and the SNR degradation, given by the product of the noise contributions of the coupling coil and the preamplifier (Eqs. [3]–[6]) for typical loading conditions of the HTS coil with the actual hardware parameters. In the case of the copper coil, the SNR is degraded by about 0.96 dB with no significant offset-frequency dependence.

#### SNR Calibration Phantom

The phantom (Fig. 3) was made of two parts: a catheter filled with distilled water and a 500-ml saline perfusion bag. NaCl concentration in the perfusion bag was adjusted in order to produce a set of different RF loading conditions; i.e., 0 mM (distilled water), 38.5 mM, 115 mM, and 154 mM. The catheter served as an absolute reference for signal calibration. Its inner diameter of 1.6 mm was kept small compared to the imaged slice thickness, so it could be assumed to give a well-defined effective voxel volume with negligible slice-shape distortions even in the nonlinear regime of the HTS coil.

#### Animals

A total of 10 nude mice of about 30 g were investigated under anesthesia induced by an intraperitoneal injection of 200  $\mu\text{L}$  of diluted (1/5) pentobarbital (Sanofi Synthelabo Laboratory, Paris, France). High-grade human mammary

tumor cells from the metastatic ductal adenocarcinoma line MDA-MB-435 (39) were subcutaneously injected on the side of the nude mice 44 days before imaging. A total of three different anatomical sites (head, back, knee) were also investigated in normal nude mice. All mice were inserted into a 24-mm-diameter plastic tube that was longitudinally slotted to provide easy and accurate positioning of the region of interest (ROI). The distance between the surface of the body and either the HTS or the copper coil was set to the respective 2- or 1-mm minimum imposed by the hardware.

Immediately after imaging, the mice were euthanized with an intraperitoneal injection of a pentobarbital overdose. The tumors were collected, kept into diluted (1/10) formaldehyde, then cut into 3- $\mu$ m-thick sections with a microtome and stained with hematoxylin-eosin safran (HES). Histological slices were performed parallel to MRI slices to allow for spatial correlation.

### Imaging Protocols

MR phantom images were acquired for both coils using identical settings and the same imaging protocols. A 2D spin-echo sequence was applied with TR/TE = 500 ms/35 ms, matrix size =  $512 \times 512$ , FOV =  $20 \times 20$  mm<sup>2</sup>, BW = 15.3 Hz/pixel, and axial slice thickness = 3 mm. The transmit level was manually adjusted with a TR of 2 s in order to achieve the maximum signal in the target ROI defined inside the capillary tube (Fig. 3).

Mice were imaged by 3D and 2D gradient-recalled acquisition in steady-state (GRASS) sequences with parameters reported in Table 1. The transmit level was adjusted during scout acquisition with a similar 2D spin-echo protocol as used for the phantom images in order to achieve the maximum signal at a 1–2-mm depth below the surface. The flip angle values reported in Table 1 were those displayed by the console corresponding to the transmit power level, but they did not account for the nonlinear behavior of the HTS coil. Thus, the values are rough, but reproducible, estimates of the actual angles in the GRASS sequences. Contrast enhancement was achieved for both knee and tumor acquisitions by manual injection of an intravenous bolus of 0.3 mmol/kg gadolinium-tetraazacyclododecane tetraacetic acid (Gd-DOTA) (Dotarem®, Guerbet, France) through a catheter in the tail vein. Contrast uptake was followed up at different spatial and temporal resolutions.

### SNR Measurements

SNR measurements for the phantoms were extracted from magnitude images using the average signal intensity over the target ROI in the capillary tube and the standard deviation in the background ROI (Fig. 3). The target ROI was closer to the copper coil by about 1 mm, corresponding to the cryogenic insulation gap only required for the HTS coil. This is a crucial point for a fair SNR comparison because of the decrease in the sensitivity profile along the coil axis. When the noise was not homogenous over the image, the background ROI was set into the lowest-noise region along the frequency-encoding axis. This position roughly corresponded to the measured matching frequency, as explained in the RF Coils section.

SNR extractions for the mice were also performed on amplitude images with the same analysis as for the phantoms and the target ROIs indicated in Fig. 4.

## RESULTS

### SNR Gains

The quality factors of the HTS and copper coils, loaded by the saline phantoms at different concentrations, are reported in Table 2. The expected SNR gain for HTS vs. copper at the matching frequency, derived from Eqs. [1], [3], and [4] for these measured quality factors, is reported in Fig. 5. With respect to the actual noise from the preamplifier and from the coupling coil, the maximum expected SNR gain achieved with the non-saline phantom is  $17.1 \pm 2.4$ . Assuming a perfect system with both a noiseless preamplifier and a noiseless coupling coil, the maximum SNR gain would have been  $21.1 \pm 2.7$ .

The measured SNR gain, averaged over six phantom images acquired with the same conditions for each coil and each saline concentration, is also reported in Fig. 5. The results agree with the expected SNR gain for all loading conditions explored here; i.e., for a quality factor of the HTS coil ranging from 845 to 13,700. A maximum measured SNR gain of  $16.7 \pm 0.1$  is achieved with the non-saline phantom.

The combination of Eqs. [1], [3], and [4] can also yield an estimation of  $T_N$  according to the measured SNR. For this purpose,  $Q_i$  for the copper coil was analytically expressed as a function of  $Q_i$  for the HTS coil, while assuming that  $1/Q_i - 1/Q_u$  only depends on the load since both coils have identical geometries. The best fit plotted in Fig. 5 was

Table 1  
Parameters of Protocols Implemented to Image the Different Mouse Sites

Protocols	TR/TE (ms)	Acquisition matrix	Acquisition bandwidth (Hz/pixel)	Flip angle (degrees)	FOV (mm <sup>3</sup> )	$t_{acq}$ (min)	Dynamic follow-up (number of consecutive loops)
Brain 1	100/8	$256 \times 128 \times 124$	61.015	90	$30 \times 15 \times 14.5$	27.3	—
Brain 2	150/25	$512 \times 256 \times 60$	30.5	90	$30 \times 15 \times 18$	41	—
Back	200/25	$512 \times 256 \times 60$	30.5	25	$30 \times 15 \times 15$	54.6	—
Knee	50/15	$512 \times 384 \times 60$	30.5	70	$30 \times 22.5 \times 18$	20	—
Tumor 1	13.9/4.8	$128 \times 64 \times 1$	61.015	70	$30 \times 15 \times 2$	0.015	100
Tumor 2	50/15	$512 \times 256 \times 28$	30.5	70	$30 \times 15 \times 8.4$	6.9	7
Tumor 3	57/14	$512 \times 256 \times 60$	30.5	70	$30 \times 15 \times 3.6$	15.6	—

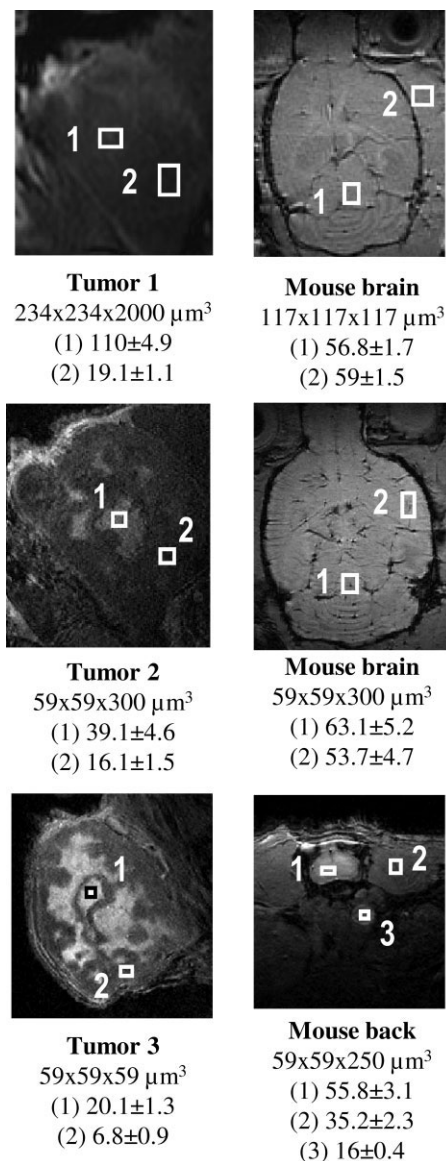


FIG. 4. ROI locations in mouse images with corresponding voxel dimensions and SNR values.

reached at a  $T_N$  of 68 K, in good agreement with the  $57 \pm 15$  K dual-temperature measurement.

SNR gains expected from the in vivo  $Q$  measurements at the different anatomical sites are reported on Table 3 and on Fig. 5 for both the ideally noiseless and the actual acquisition system. In the actual case, typical gains were 9.8, 9.8, 5.4, and 11.6 for the brain, knee, back, and subcutaneous implanted tumors, respectively.

The nonuniformity of the background noise with HTS-coil acquisitions was easily visible at large frequency offsets and was more pronounced with decreasing sample losses, in quite fair agreement with the theory. Figure 6 depicts the background-noise profile along the frequency-encoding axis of an image acquired without any sample, i.e., the most sensitive situation, after a particularly careful adjustment of the tuning and matching conditions.

## In-Vivo Imaging

Typical in vivo data acquired with the HTS coil following the protocols given in Table 1 are displayed in Figs. 7–9 for different anatomical sites and in Figs. 10–12 for tumor explorations. Set voxel dimensions and the measured SNR for the different sites are reported in Fig. 4.

Images of the mouse brain obtained with Brain 1 and Brain 2 protocols at about the same anatomical level are presented in Fig. 7 with regard to a corresponding plate of the mouse brain atlases (40). Brain structures such as the ventricles, corpus callosum, hippocampus, and cerebellum with internal gray/white matter differentiation, are well identified with Brain 1. Noticeably in the hippocampus, regions of higher cell densities such as the CA3 and dentel gyrus are depicted by their hypersignal. The cerebral microvasculature is strongly enhanced in the Brain 2 view with long TE (25 ms) and small voxel size ( $59 \times 59 \times 300 \mu\text{m}^3$ ).

The mouse back view (Fig. 8) allows the discrimination of gray and white matter within the spinal cord with a contrast-to-noise ratio of about 15. Although the protocol incorporates neither flow-compensation nor cardiac synchronization, the aorta is already well delimited with a SNR of 16 at a 5-mm depth inside the mouse body.

Figure 9 reveals articular structures in the knee of a mouse 40 min after the injection of Gd-DOTA.

Figures 10 and 11 illustrate the contrast uptake dynamics inside a tumor before and after injection of Gd-DOTA, with protocols Tumor 1 and Tumor 2, respectively. The profiles for a given ROI have been computed as where  $SI_{pre}$  and  $SI_{post}$  are the pre- and postinjection signal intensities, respectively. Protocol Tumor 1 allows the characterization of different areas within the tumor by following the first arrival of the contrast agent at a time resolution of 0.9 s and a SNR ranging from 100 to 300. Protocol Tumor 2, based on  $59 \times 59 \times 300 \mu\text{m}^3$  voxels, has a lower time resolution of 6.9 min but a volume resolution 100 times better than protocol Tumor 1. The sharply-delimited tumor heterogeneities show different dynamical behaviors over the 1-h investigation as plotted in Fig. 11. Protocol Tumor 3, started after a 1-h delay following the Gd-DOTA injection, achieves even higher volume resolution with a  $59\text{-}\mu\text{m}$  isotropic voxel size. This protocol helps to structural heterogeneities as different tumor components by confrontation with histology (Fig. 12). All tumors are characterized as high-grade carcinomas, poorly differentiated and necrotic in approximately 50% of the volume. Some tumors exhibit typical features such as central necrosis with no cells, microcalcifications, microinfiltrations, and tumoral

Table 2  
Measured Quality Factors of the HTS and Copper Coils Loaded by the Saline Phantom With Different Concentrations

Phantoms [NaCl]	Loaded quality factors	
	HTS coil	Copper coil
0 mM	13700 $\pm$ 200	111 $\pm$ 11
38.5 mM	2854 $\pm$ 40	106 $\pm$ 10
115 mM	1150 $\pm$ 20	105 $\pm$ 10
154 mM	845 $\pm$ 10	102 $\pm$ 10

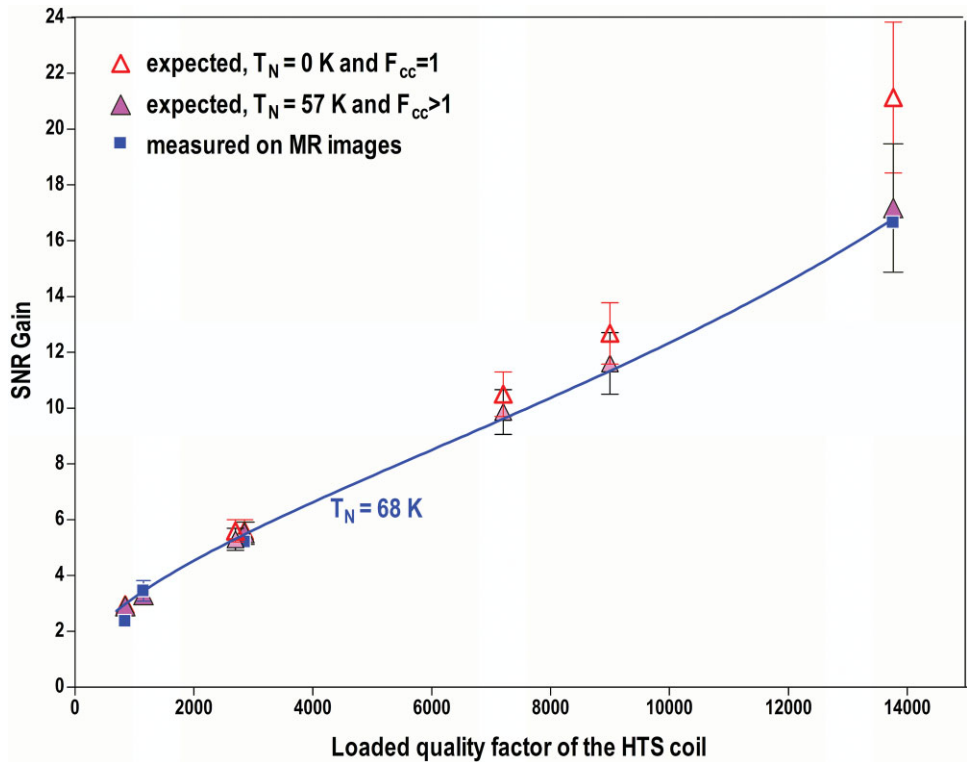


FIG. 5. Expected and actual SNR gains as a function of the loaded quality factor of the HTS coil. The SNR gain expectation either assumes a noiseless preamplifier and coupling coil ( $T_N = 0$  K and  $F_{cc} = 1$ ) or accounts for their actual noise ( $T_N = 57$  K and  $F_{cc} > 1$ ) as given by Eqs. [3]–[6]). The error bars include the uncertainty on the  $Q_l$  and  $T_N$  measurements. The measured data are fitted using Eq. [1] combined with Eq. [3] with the least error at  $T_N = 68$  K.

microvessels, which were also visible on the MR images. Gd-DOTA accumulates in necrotic areas within the first 10 min. Living tumoral tissue, necrosis, and well-vascularized, granulated nontumoral tissue correspond to different Gd-DOTA uptake dynamics.

**DISCUSSION**

This is the first report of in vivo SNR enhancements by more than an order of magnitude using a surface coil made of HTS material as compared with a room-temperature copper coil of similar geometry. The diameter of both surface coils was 12 mm and the comparison was undertaken for the particular situation of mouse imaging in a standard 1.5T body scanner. The only difference between the coils was the 15- $\mu$ m electrodeposited copper layer instead of the 400-nm YBaCuO film employed to elaborate the windings. Both thicknesses were assumed to correspond to nearly optimum RF performances for each mate-

rial. The coils were positioned as close as possible to the sample surface according to the mechanical and cryogenic constraints respective to each setup. Overall acquisition conditions are thought by the authors to make an unbiased comparison as fair as possible.

Assuming a noiseless coupling circuit and preamplifier with a negligibly conductive sample, the HTS coil device cooled to 80 K in the present evaluation can achieve an ultimate SNR gain of about 21 with respect to the similar room-temperature copper coil. For comparison, cooling the copper coil to 80 K would have achieved a maximum SNR gain of 3.2, assuming an increase of conductivity by a factor of 8.5 (i.e., a 2.9-times higher unloaded quality fac-

Table 3  
Measured Quality Factors of the HTS and Copper Coils Loaded by the Different Anatomical Sites of the Mouse In Vivo\*

Mouse sites	Loaded quality factors		Expected SNR gains	
	HTS coil	Copper coil	$T_N = 0$ K and $F_{cc} = 1$	$T_N = 57$ K and $F_{cc} > 1$
Head	7,200 $\pm$ 108	106 $\pm$ 10	10.5 $\pm$ 0.8	9.8 $\pm$ 0.8
Back	2,700 $\pm$ 40	105 $\pm$ 10	5.4 $\pm$ 0.4	5.4 $\pm$ 0.9
Knee	7,200 $\pm$ 108	106 $\pm$ 10	10.5 $\pm$ 0.8	9.8 $\pm$ 0.8
Tumor	9,000 $\pm$ 135	107 $\pm$ 10	12.7 $\pm$ 1.1	11.6 $\pm$ 1.1

\*Corresponding SNR gains are derived from Eq. [1] and Eq. [3], either assuming a perfectly noiseless preamplifier and coupling coil, or accounting for the actual noise from both.

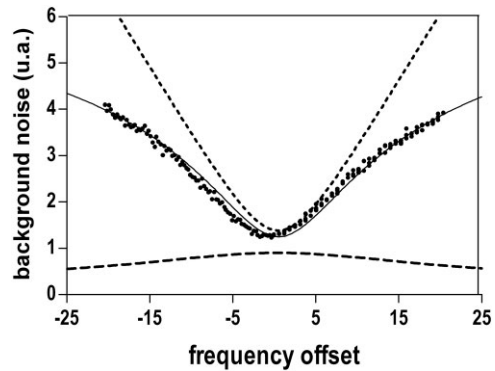


FIG. 6. Measured background-noise profile with the unloaded HTS coil ( $Q_L = 13,700$ ). The standard deviation (dots) is measured along the frequency-encoding axis of the image. It is compared with the expected profile (plain curve) computed from the receiver gain flatness (lower dashed curve) and SNR degradation (upper dashed curve) also displayed on Fig. 2.

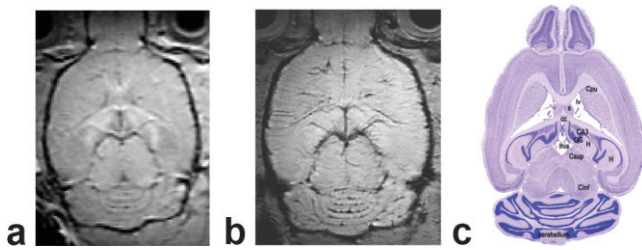


FIG. 7. In vivo coronal mouse brain slices. The images have been acquired with protocols Brain 1 (a) and Brain 2 (b) before being cropped by a factor of 2. Section 157 (c) is from the mouse brain atlas (40). Structures such as the forceps major of the corpus (fmi), corpus callosum (cc), adrenaline cells (CA), hippocampus (H), left ventricle (lv), dentate gyrus (DG), Culliculi inferior and superior (C-inf and C-sup), and longitudinal hippocampal artery (lhia) can be identified on the MR images. See protocol details on Table 1 and local SNR measurements on Fig. 4. [Color figure can be viewed in the online issue, which is available at <http://www.interscience.wiley.com>.]

tor) with extremely pure copper (41,17). The ultimate SNR gain is limited by the performance of the superconducting material, which is conjointly affected by the ambient 1.5T field and 80 K temperature. Still, in view of investigating very small or low-conductive samples, further improving the SNR by lowering the HTS coil temperature might be possible. However, the warm coupling coil and preamplifier would rapidly limit the improvement since they already attenuate the SNR gain significantly at 80 K, by about 20% at the tuning frequency and 60% at  $\pm 8$ -kHz frequency offsets.

Rather than weakly conductive or small biological samples, this work investigated anatomical areas of the mouse where the sample noise still dominates the coil noise.

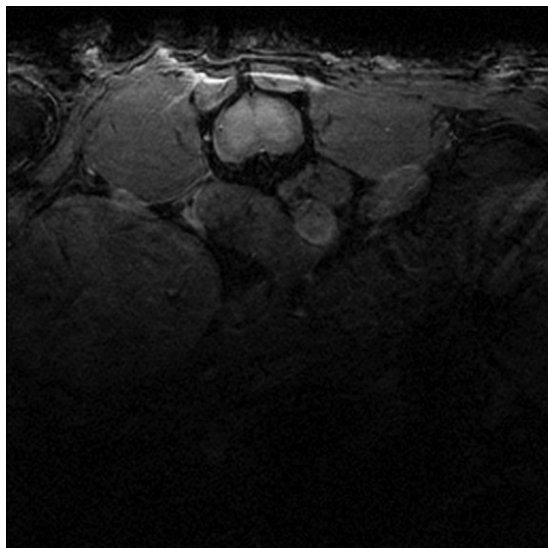


FIG. 8. In vivo axial slice of a mouse back. The image has been acquired with protocol Back before being cropped by a factor 2. With a  $T_1$  contrast, it is possible to discern gray and white matter at the spinal cord of the animal. The aorta is well depicted at a depth of about 5 mm. See protocol details on Table 1 and local SNR measurements on Fig. 4.

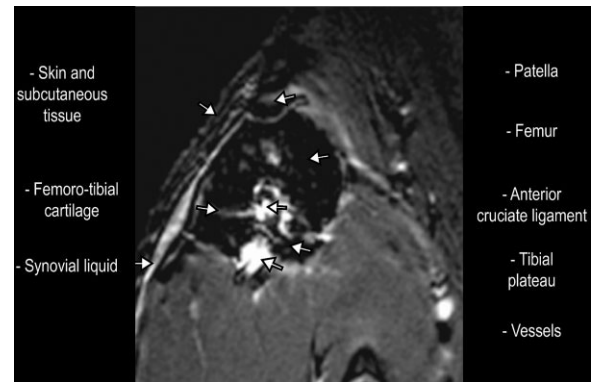


FIG. 9. In vivo axial slice of a mouse knee. The image has been acquired with the protocol Knee 40 min after a Gd-DOTA injection and cropped by a factor of  $4 \times 4.3$ . The synovial fluid is strongly enhanced as compared with before the injection (not shown). See protocol details on Table 1.

Therefore, only marginal extra SNR gains can be expected at the tuning frequency with additional coil or preamplifier improvements. According to the theory, a perfect noiseless RF coil (e.g., with null  $T_c$ ) combined with a noiseless preamplifier and coupling devices would ultimately increase the SNR gain up to 13.4 instead of the present 11.6 for the case of subcutaneously implanted tumors, which corresponds to the highest quality factor (9000) encountered in the in vivo study. However, the mouse tumors were investigated with a 30-mm readout FOV, corresponding to a total  $\pm 8$ -kHz BW. According to Fig. 2, the image SNR would be degraded by a factor of 0.69 at the edges of the FOV relative to the center. Nevertheless, by carefully centering the tumor in the lowest-noise region of the FOV, the high SNR is maintained within a few percent over the tumor width, which generally does not exceed 10 mm. Besides, the image is already filtered out above  $\pm 4$ -kHz since the spatial sensitivity map

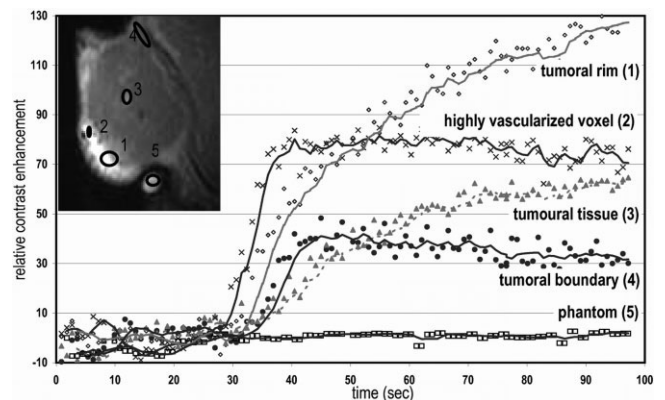


FIG. 10. Contrast uptake over time during the perfusion phase of a subcutaneously implanted tumor in the mouse. The analysis has been done with a series of images acquired with protocol Tumor 1. The contrast-enhancement kinetics allows the discrimination of areas in the tumor that correspond to tumoral rim, excavated necrosis, and highly vascularized tissue. The reference signal is given by a tubular phantom filled with distilled water. See protocol details on Table 1 and local SNR measurements on Fig. 4.

of the HTS coil itself does not extend much further than  $\pm 8$  mm. At  $\pm 4$ -kHz offsets, the SNR is degraded by 10% compared to the lowest-noise offset.

Cooling the electronics would be needed to access larger acquisition BWs while maintaining the high SNR provided by HTS coil along the readout FOV. The improvement brought by integrating the coupling coil and a custom preamplifier in the cryostat can readily be evaluated using the set of equations in the Theory section. For example, in the crucial case of mouse tumors, the HTS probehead would provide an SNR gain of 13.4 at the center of the readout FOV by assuming a coupling coil made of pure copper at 80 K and a preamplifier featuring a noise temperature of 15 K are used. The sideband SNR gain of 12.9 at  $\pm 4$  kHz would be kept above 10 at frequency offsets up to  $\pm 16$  kHz.

The HTS coil diameter of 12 mm is well suited to study a large variety of anatomical sites in mice. An exploration depth of about 5 mm is already accessible with the presented protocols based on transmit-receive and small flip-angle gradient-echo modes. The MR signal intensity almost depends on the coil sensitivity squared through the cumulative effect of transmission and reception. By decoupling the HTS coil to operate it in receive-only mode, spatially uniform excitation pulses could be independently applied with a larger transmit coil and the penetration depth would be increased since it would be limited only by reception. Full coverage of the mouse body could finally be achieved with an array based on 12-mm receive-only HTS elements maintaining the same SNR enhancement shown locally in this study.

Another issue with the transmit-receive operation of the HTS surface coil is the significant variation of the applied flip angle over the image FOV. Therefore, spin-echo protocols in the phantom studies could only be exploited over a restricted ROI. Instead, the *in vivo* investigations were all based on gradient-echo protocols and covered larger areas at the cost of a nonuniformly weighted  $T_1$  contrast. With receive-only HTS coil operation, the  $T_1$  contrast would be

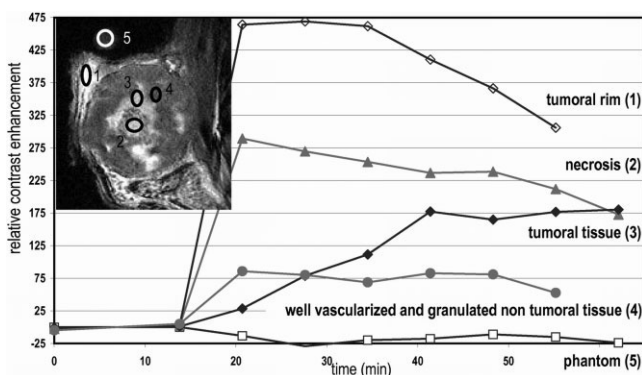


FIG. 11. Contrast uptake over time during the leakage phase of a subcutaneously implanted tumor in the mouse. The analysis was done on a series of images acquired with protocol Tumor 2. Different dynamic behaviors are exhibited during the 1-h investigation corresponding to tumoral rim, excavated necrosis, and highly vascularized tissue. The reference signal is given by a tubular phantom filled with distilled water. See protocol details on Table 1 and local SNR measurements on Fig. 4.

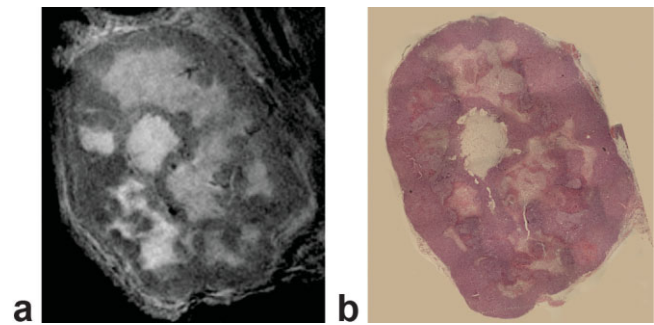


FIG. 12. Comparison of a high resolution slice (a) to the corresponding 3- $\mu$ m-thick histological slice (b) in a subcutaneously implanted tumor in the mouse. The isotropic MR image has been acquired with protocol Tumor 3 an hour after Gd-DOTA injection. The comparison yields the identification of different tumor components, such as living tumoral tissue, necrosis, and well-vascularized nontumoral tissue, as a basis of the structural heterogeneities visible on the MR image. See protocol details on Table 1 and local SNR measurements on Fig. 4. [Color figure can be viewed in the online issue, which is available at <http://www.interscience.wiley.com>.]

better assessed, spin-echo sequences would be easily implemented, and  $T_2$  contrast would be available. HTS coil decoupling is thus a primary focus for further development.

Although there are still implementation issues as discussed above, using a small HTS coil was determinant in achieving high-quality mouse images with 1.5T. The SNR advantage could be converted into substantial spatial or temporal resolution improvements. Small voxels are needed to accurately evaluate neovascular components and potentially differentiate malignant from benign tumors based on dynamic contrast enhancement (42). The 0.2-nL resolution, achieved with a SNR of 20 in subcutaneous tumors with protocol Tumor 3, is a key feature to discriminate tissue components that could be accurately correlated with histology. The subsecond temporal resolution, reached here with protocol Tumor 1 at less than 250- $\mu$ m in-plane resolution, can bring complementary first-arrival perfusion information regarding angiogenesis processes (43). In the brain images (Fig. 7), voxel sizes were small enough to reach a partial-volume regime where individual microvessels were made observable through their  $T_2^*$  effect, which extends to larger spatial scales as imaged. Subnanoliter resolution combined with a pertinent contrast mechanism is generally required to discriminate subregions within the hippocampus (44). In the present investigation, at relatively low field, this is afforded by the  $T_1$ -weighted protocol Brain 1.

The very sensitive RF detection provided by the HTS coil in the present work at 1.5T leads to resolution levels that are usually encountered with high-field MR microscopes. The protocols here were generally based on narrow acquisition BWs that are not convenient in high-field investigations, because of susceptibility and chemical-shift artifacts, but they contribute to improving the SNR in addition to the gain brought by the HTS coil itself. Besides, no individual shimming procedure was applied to reduce field heterogeneities. Nevertheless, implementation of cryogenically-operated coils at high fields can substan-

tially enhance the SNR. A recent work with a cooled copper coil at 9.4T demonstrated a SNR gain of 2.4 for in vivo brain images of mice (22). A gain of 7.0 was reported earlier at 9.4T involving a HTS coil to explore excised mouse kidneys (19). However, developing in vivo applications with HTS probes for such high-field, small-bore systems remains a challenging issue due to the lack of room to handle the animal and insert the cryogenic setup. Lower operating temperatures are required to maintain the superconducting performance of the HTS material (17), and a cold screen surrounding the RF coil is needed since electromagnetic coupling with warm external structures can induce a significant amount of thermal noise (45).

In conclusion, the principal argument in favor of the HTS coil approach presented in this work is the ability to reach high spatial and temporal resolutions needed for small animal investigations without necessarily needing an increased magnetic field. Cryogenically-operated RF coils could offer the biomedical experimenter an extended opportunity to choose the adequate field intensity and find a compromise with resolution and contrast-to-noise for any particular application or pathology domain.

## ACKNOWLEDGMENTS

We thank the team at the Center for Inter-Establishment Magnetic Resonance (CIERM), Hôpital de Bicêtre (Bicêtre, France), for their help with the 1.5T platform, plus Emmanuelle Canet, Marc Dhenain, Astrid Pinzano, Pierre Gillet, and Damien Lœille for useful discussions about the mouse images.

## REFERENCES

- Henkelman RM, van Heteren JG, Bronskill MJ. Small animal imaging with a clinical magnetic resonance imager. *Magn Reson Med* 1987;4: 61–66.
- Button TM, Fiel RJ, Goldrosen M, Paolini N. Small animal MRI at 0.35 Tesla: growth and morphology of intra-organ murine tumors. *Magn Reson Imaging* 1990;8:505–509.
- Smith DA, Clarke LP, Fiedler JA, Murtagh FR, Bonaroti EA, Sengstock GJ, Arendash GW. Use of a clinical MR scanner for imaging the rat brain. *Brain Res Bull* 1993;31:115–120.
- Guzman R, Lovblad KO, Meyer M, Spenger C, Schroth G, Widmer HR. Imaging the rat brain on a 1.5 T clinical MR-scanner. *J Neurosci Methods* 2000;97:77–85.
- Graf H, Martirosian P, Schick F, Grieser M, Bellemann ME. Inductively coupled RF coils for examinations of small animals and objects in standard whole-body MR scanners. *Med Phys* 2003;30:1241–1245.
- Chen F, Suzuki Y, Nagai N, Peeters R, Coenegrachts K, Coudyzer W, Marchal G, Ni Y. Visualization of stroke with clinical MR imagers in rats: a feasibility study. *Radiology* 2004;233:905–911.
- Oweida AJ, Dunn EA, Foster PJ. Cellular imaging at 1.5 T: detecting cells in neuroinflammation using active labeling with superparamagnetic iron oxide. *Mol Imaging* 2004;3:85–95.
- Pfefferbaum A, Adalsteinsson E, Sullivan EV. In vivo structural imaging of the rat brain with a 3-T clinical human scanner. *J Magn Reson Imaging* 2004;20:779–785.
- Beuf O, Jaillon F, Saint-Jalmes H. Small-animal MRI: signal-to-noise ratio comparison at 7 and 1.5 T with multiple-animal acquisition strategies. *MAGMA* 2006;19:202–208.
- Brockmann MA, Ulmer S, Leppert J, Nadrowitz R, Wuestenberg R, Nolte I, Petersen D, Groden C, Giese A, Gottschalk S. Analysis of mouse brain using a clinical 1.5 T scanner and a standard small loop surface coil. *Brain Res* 2006;1068:138–142.
- Heyn C, Ronald JA, Ramadan SS, Snir JA, Barry AM, MacKenzie LT, Mikulis DJ, Palmieri D, Bronder JL, Steeg PS, Yoneda T, MacDonald IC, Chambers AF, Rutt BK, Foster PJ. In vivo MRI of cancer cell fate at the single-cell level in a mouse model of breast cancer metastasis to the brain. *Magn Reson Med* 2006;56:1001–1010.
- Arai T, Kofidis T, Bulte JW, de Bruin J, Venook RD, Berry GJ, McConnell MV, Quertermous T, Robbins RC, Yang PC. Dual in vivo magnetic resonance evaluation of magnetically labeled mouse embryonic stem cells and cardiac function at 1.5 T. *Magn Reson Med* 2006;55:203–209.
- Lee FK, Fang MR, Antonio GE, Yeung DK, Chan ET, Zhang LH, Yew DT, Ahuja AT. Diffusion tensor imaging (DTI) of rodent brains in vivo using a 1.5T clinical MR scanner. *J Magn Reson Imaging* 2006;23:747–751.
- Pirko I, Fricke ST, Johnson AJ, Rodriguez M, Macura SI. Magnetic resonance imaging, microscopy, and spectroscopy of the central nervous system in experimental animals. *NeuroRX* 2005;2:250–264.
- Schmiedl UP, Maravilla KR, Nelson JA. Improved method for in vivo magnetic-resonance contrast-media research. *Invest Radiol* 1991;26: 65–70.
- Bock NA, Konyer NB, Henkelman RM. Multiple-mouse MRI. *Magn Reson Med* 2003;49:158–167.
- Darrasse L, Ginefri, J.C. Perspectives with cryogenic RF probes in biomedical MRI. *Biochimie* 2003;85:915–937.
- Black RD, Early TA, Johnson GA. Performance of a high-temperature superconducting resonator for high-field imaging. *J Magn Reson A* 1995;113:74–80.
- Hurlston SE, Brey WW, Suddarth SA, Johnson GA, Fitzsimons EG. A high-temperature superconducting Helmholtz probe for microscopy at 9.4 T. *Magn Reson Med* 1999;41:1032–1038.
- Miller JR, Hurlston SE, Ma QY, Face DW, Kountz DJ, MacFall JR, Hedlund LW, Johnson GA. Performance of a high-temperature superconducting probe for in vivo microscopy at 2.0 T. *Magn Reson Med* 1999;41:72–79.
- Wosik J, Wang F, Xie L-M, Strikovski M, Kamel M, Nesteruk K, Bilgen M, Narayana PA. High-Tc superconducting surface coil for 2 Tesla magnetic resonance imaging of small animals. *IEEE T Appl Supercon* 2001;11:681–684.
- Haueisen R, Marek D, Sacher M, Ugurbil K, Junge S. Flexible cryo-probe-setup for mice brain imaging and spectroscopy at 9.4T. Basel, Switzerland, 15–18 September 2005. *Magn Reson Mat Biol Phys Med*. p S147.
- Wright AC, Hee Kwon S, Wehrli FW. In vivo MR micro imaging with conventional radiofrequency coils cooled to 77°K. *Magn Reson Med* 2000;43:163–169.
- Lee HL, Lin IT, Chen JH, Horng HE, Yang HC. High-T-c superconducting receiving coils for nuclear magnetic resonance imaging. *IEEE T Appl Supercon* 2005;15:1326–1329.
- Kwok WE, You ZG. In vivo MRI using liquid nitrogen cooled phased array coil at 3.0 T. *Magn Reson Imaging* 2006;24:819–823.
- Ginefri JC, Darrasse L, Crozat P. High-temperature superconducting surface coil for in vivo microimaging of the human skin. *Magn Reson Med* 2001;45:376–382.
- Poirier-Quinot M, Ginefri J-C, Darrasse L, Ledru F, Fornes P. Preliminary ex-vivo 3D microscopy of coronary arteries using a standard 1.5T MRI scanner and a HTS RF probe. *MAGMA* 2005;18:89–95.
- Poirier-Quinot MG, Ginefri JC, Robert P, Darrasse L. Feasibility of in vivo microimaging of the mouse in a conventional 1.5 T body scanner equipped with a 12 mm HTS surface coil. In: Proceedings of the 12th Annual Meeting of ISMRM, Kyoto, Japan, 2004 (Abstract 1754).
- Robert P, Poirier-Quinot M, Bruneval P, Violas X, Santus R, Ginefri JC, Darrasse L, Corot C. In vivo assessment of tumor heterogeneity in Mouse: comparison between a blood pool and a conventional extracellular contrast agents by tumoral 3D-microimaging at 1.5 T. In: Proceedings of the 12th Annual Meeting of ISMRM, Kyoto, Japan, 2004 (Abstract 1983).
- Ginefri JC, Poirier-Quinot M, Robert P, Darrasse L. Contrast-enhanced dynamic MRI protocol with improved spatial and time resolution for in vivo microimaging of the mouse with a 1.5-T body scanner and a superconducting surface coil. *Magn Reson Imaging* 2005;23:239–243.
- Adler R, Espersen G. Description of the noise performance of amplifiers and receiving systems. *Proc IEEE* 1963;51:436–442.

32. Jerosch-Herold M, Kirschman R. Potential benefits of a cryogenically cooled NMR probe for room-temperature samples. *J Magn Reson* 1989; 85:141–146.
33. Raad A, Darrasse L. Optimization of NMR receiver bandwidth by inductive coupling. *Magn Reson Imaging* 1992;10:55–65.
34. Suddarth S. A method for matching high-temperature superconductor resonators used for NMR signal pickup at 400 MHz. *IEEE Trans Biomed Eng* 1998;45:1061–1060.
35. Roemer PB, Edelstein WA, Hayes CE, Souza SP, Mueller OM. The NMR phased array. *Magn Reson Med* 1990;16:192–225.
36. Serfaty S, Haziza N, Darrasse L, Kan S. Multi-turn split-conductor transmission-line resonators. *Magn Reson Med* 1997;38:687–689.
37. Lemaitre Y, Mercandalli LM, Dessertenne B, Mansart D, Marcilhac B, Mage JC. Large-area high-quality ybco thin-films by inverted cylindrical magnetron technique. *Physica C* 1994;235:643–644.
38. Coutrot A-L, Dufour-Gergam E, Quemper J-M, Martincic E, Gilles J-P, Grandchamp J-P, Matlosz M, Sanchez A, Darasse L, Ginefri J-C. Copper micromoulding process for NMR microinductors realization. *Sens Actuators A Phys* 2002;99:49–54.
39. Cailleau R, Young R, Olivé M, Reeves WJ Jr. Breast tumor cell lines from pleural effusions. *J Natl Cancer Inst* 1974;53:661–674.
40. Paxinos G, Franklin KBJ. *The mouse brain in stereotaxic coordinates*. San Diego: Academic Press; 2001.
41. Powel RL, Fickett FR. *Cryogenic properties of copper*. Boulder, CO: National Bureau of Standards; 1979.
42. Aref M, Brechbiel M, Wiener EC. Identifying tumor vascular permeability heterogeneity with magnetic resonance imaging contrast agents. *Invest Radiol* 2002;37:178–192.
43. de Bazelaire C, Siauve N, Fournier L, Frouin F, Robert P, Clement O, de Kerviler E, Cuenod CA. Comprehensive model for simultaneous MRI determination of perfusion and permeability using a blood-pool agent in rats rhabdomyosarcoma. *Eur Radiol* 2005;15:2497–2505.
44. Benveniste H, Blackband S. MR microscopy and high resolution small animal MRI: applications in neuroscience research. *Prog Neurobiol* 2002;67:393–420.
45. Odoj F, Rommel E, v Kienlin M, Haase A. A superconducting probe-head applicable for nuclear magnetic resonance microscopy at 7 T. *Rev Sci Instrum* 1998;69:2708–2712.